Translational Oncology 68 (2026) 102765

Contents lists available at ScienceDirect

Translational Oncology

journal homepage: www.elsevier.com/locate/tranon

Integrated spatial and single-cell transcriptomics maps disulfidptosis in renal cell carcinoma and reveals PDLIM1 as a prognostic biomarker and potential therapeutic target

Wenqiang Liu [a,1], Xianglin Liu [b,1], Juan Yi [c,1], Zhao Tang [a,1], Ziwen Dai [a,1], Jiaao Song [a], Tong Chen [a], Jun Wang [a], Jiaxuan Wang [a], Wentao Jiang [a], Aimin Jiang [a,c,*], Zhenjie Wu [a,*], Lifang Tang [a,c,**], Yuming Jin [a,c,**], Yinghu Chen [a,c,**], Linhui Wang [a,*]

[a] Department of Urology, Changhai Hospital, Navel Medical University (Second Military Medical University), Shanghai, China
[b] Department of General Surgery, 921 Hospital of Joint Logistics Support Force People's Liberation Army of China, China
[c] Department of Urology, The First Naval Hospital of Southern Theater Command, Zhanjiang, China

ARTICLE INFO

Keywords:
Renal cell carcinoma
Spatial transcriptomics
scRNA-seq
Disulfidptosis

ABSTRACT

Background: Disulfidptosis is a regulated cell death program linked to redox stress, metabolism, and the actin cytoskeleton. Its organization in tissue and clinical relevance in renal cell carcinoma are not well defined.
Methods: We integrated spatial transcriptomics from six renal cancer sections with four single cell RNA sequencing cohorts. Disulfidptosis scores were computed, RCTD deconvolution and epithelial reclustering were used to localize subpopulations, and pathway enrichment and CytoTRACE assessed metabolism and stemness. External validation used TCGA-KIRC, KIRP and additional public datasets. Candidate genes were nominated by intersecting disulfidptosis, Cluster 3, and Epi_C5 signatures. PDLIM1 function was tested by sh-RNA in renal cancer cell lines with qPCR, proliferation, wound healing, and Transwell assays.
Results: Disulfidptosis showed strong intra heterogeneity. Spatial clusters 2, 3, and 6 were enriched, with Cluster 3 higher in tumors and linked to worse survival, and Cluster 6 context dependent yet adverse. Signals localized mainly to epithelial cells. Epithelial reclustering identified Epi_C5 with the highest disulfidptosis and Cluster 3 scores. Disulfidptosis-high cells were enriched for N glycan biosynthesis, purine and pyrimidine metabolism, oxidative phosphorylation, and nitrogen metabolism, with spatial overlap between nitrogen metabolism and disulfidptosis. Epi_C5 upregulated extracellular matrix programs, showed higher CytoTRACE, and associated with poor prognosis in both TCGA cohorts. Intersecting signatures nominated PDLIM1, which was tumor elevated and correlated with Epi_C5 and CytoTRACE. PDLIM1 knockdown reduced proliferation, and migration.
Conclusions: We define a disulfidptosis-associated epithelial malignant state in renal cancer and nominate PDLIM1 as a candidate node for patient stratification and therapeutic development.

Introduction

Renal cell carcinoma (RCC) exhibits pronounced molecular and spatial heterogeneity [1–3] that shapes tumor evolution, metastatic routes, and clinical outcomes [4–8]. Multi-region and longitudinal sampling from the TRACERx Renal program delineated deterministic evolutionary trajectories in clear cell RCC (ccRCC) and linked chromosomal complexity to metastatic competence and mortality [9–12]. At the subtype level, TCGA atlases for ccRCC (KIRC) and papillary RCC (KIRP) established the genomic drivers, metabolic rewiring, and clinical correlates that underlie the emerging view of RCC as a metabolically reprogrammed disease [13,14]. Nevertheless, despite targeted agents and immune checkpoint inhibitors [15,16], a substantial subset of patients experiences progression, underscoring the need to

* Corresponding author: Department of Urology, Changhai Hospital, Naval Medical University, 168 Changhai Road, Shanghai 200433, China.
** Corresponding author: Department of Urology, The First Naval Hospital of Southern Theater Command, Zhanjiang, China.
E-mail addresses: czjiangaimin@smmu.edu.cn (A. Jiang), wuzhenjie17@163.com (Z. Wu), 285270883@qq.com (L. Tang), jinyuming5478@126.com (Y. Jin), 1476669205@qq.com (Y. Chen), wanglinhui@smmu.edu.cn (L. Wang).
[1] Those authors contributed equally.

https://doi.org/10.1016/j.tranon.2026.102765
Received 27 January 2026; Received in revised form 9 March 2026; Accepted 9 April 2026

expose actionable vulnerabilities and the cell states that harbor them.

Among newly recognized forms of regulated cell death, disulfidptosis highlights a therapeutic vulnerability at the nexus of redox stress, metabolism, and the actin cytoskeleton [17,18]. In SLC7A11 high cells, glucose deprivation or inhibition of glucose transport elevates disulfide burden [19–21], induces aberrant disulfide bonds in actin cytoskeletal proteins, and triggers F-actin collapse [22], producing a cell-death phenotype distinct from apoptosis and ferroptosis [23]. These findings suggest that nutrient availability and cytoskeletal homeostasis may cooperatively select for disulfidptosis–sensitive subpopulations within tumors.

To localize disulfidptosis in situ and dissect its microenvironmental context, integration of spatial transcriptomics (ST) with single-cell RNA-seq is essential (C [24–26]). Since its inception, ST has enabled quantitative, spatially resolved transcriptome mapping in tissue sections [8,27–29]; jointly analyzing ST with single-cell references allows robust cell-type deconvolution and spatial composition inference, while tools such as CytoTRACE [30,31] quantify stemness/immaturity at single-cell resolution to aid phenotypic interpretation.

At the molecular interface with the cytoskeleton, PDLIM1 (CLP36) is a PDZ-LIM scaffold that interacts with α-actinin and participates in stress-fiber organization and cell polarity [32,33]. Its role in cancer appears context-dependent: PDLIM1 can promote migration and metastasis [34,35] yet has also been reported to stabilize adhesion complexes or engage Hippo signaling to restrain EMT and metastasis [34,35]. These observations motivate a systematic evaluation of how disulfidptosis is spatially organized in RCC, which epithelial subpopulations are most involved, and whether cytoskeletal hubs such as PDLIM1 link disulfidptosisto malignant phenotypes.

Here we integrate multi-cohort spatial transcriptomics and single-cell datasets to chart the spatial heterogeneity and cell-type distribution of disulfidptosis in RCC, revealing prominent epithelial localization and pinpointing a malignant epithelial subpopulation linked to adverse prognosis. Intersecting disulfidptosis, Cluster-3 and Epi_C5 signatures nominates the actin-associated scaffold PDLIM1 as a candidate hub whose expression correlates with stemness, ECM/extracellular-structure programs and poor outcome. Functional perturbations via siRNA in RCC models demonstrate that PDLIM1 knockdown attenuates proliferation, clonogenicity, and migration.

Method and material

Data source and scoring

We obtained spatial transcriptomics data from GEO accession GSE175540 (six tissue sections) and four scRNA-seq samples under GSE156632 and GSE144735 to define and validate macrophage markers and provide a reference for integration with tumor epithelial subpopulations; bulk RNA-seq profiles with matched clinical metadata and somatic mutation calls were downloaded from TCGA for both KIRC and KIRP, including 72 normal renal samples and 542 KIRC tumors (with 533 KIRC cases retained after excluding those lacking survival information) and, for KIRP, 32 normal renal samples and 289 tumors; independent external validation datasets (with clinical annotations) were retrieved from GEO (GSE167573, GSE40435, GSE53757); all datasets are publicly available and did not require additional ethics approval. (pmc.ncbi.nlm.nih.gov) We curated a disulfidptosis gene set with literature provenance and initiator versus responder annotations (Supplementary Table S1) and computed sample- and cell-level scores using ssGSEA with AUCell as a sensitivity check; results were consistent across methods. For bulk and single-cell profiles, we computed per-sample/per-cell scores using ssGSEA on log-normalized counts with gene-wise scaling. As a sensitivity analysis, we computed AUCell scores with default ranking, and called “high” cells using an adaptive AUC threshold (top 10 % unless otherwise specified). Results were concordant across methods.

Cell identification by scRNA-seq and determination of cell type by multimodal intersection analysis (MIA)

We integrated the ST data with publicly available scRNA-seq data [36,37] by employing the previously reported MIA (Molecular Interaction Annotation) approach. The significance of the overlap between cell type marker genes and ST genes was identified using the hypergeometric cumulative distribution method, with all genes as the background to calculate the P values.

Spatial transcriptomics

Spatial RNA-seq data were examined utilizing the Seurat package (version 4.4.0). The process commenced with normalizing the gene expression matrix for each sample via the sctransform function. Subsequently, principal component analysis (PCA) was conducted, coupled with uniform manifold approximation and projection (UMAP) for dimensionality reduction. Clustering was discerned employing the Louvain algorithm, set with parameters dims = 20 and res = 0.2. The Wilcoxon test was applied to pinpoint differentially expressed genes (DEGs) across clusters, with stringent criteria of an adjusted P value $<$ 0.05 and a log fold change (logFC) exceeding 0.25 for gene selection as markers. To ascertain the prevalence of specific cell types within clusters, a Fisher's exact test was conducted, using all genes as a reference, to evaluate the statistical significance of the intersection between ST marker genes and those identified by scRNA-seq. This analysis allowed us to compute the odds ratio and associated P value, thereby revealing cell type enrichment patterns.

ScRNA-seq cluster analysis

Publicly available single-cell RNA sequencing (scRNA-seq) data were retrieved from the GEO database (accession number: GSE144735), which includes transcriptomic profiles of tumor and matched normal kidney tissues from patients with ccRCC. Raw count matrices were downloaded and processed using the Seurat (v4.3.0) R package. Quality control filtering was applied to exclude cells with fewer than 200 detected genes or $>$10 % mitochondrial gene expression. After normalization and scaling, highly variable genes were identified using the "vst" method, and principal component analysis (PCA) was performed for dimensionality reduction. The top 20 principal components were selected for downstream clustering using the Louvain algorithm with a resolution of 0.5. Cell clusters were visualized using Uniform Manifold Approximation and Projection (UMAP), and a total of 19 distinct clusters were identified. Cell-type annotation was performed based on canonical marker genes for major immune cell types, including B cells (CD79A), T cells (CD3D), macrophages (CD68, CD163), NK cells (NKG7), mast cells (TPSAB1), and plasma cells (MZB1).

Cell lines culture

786O cells and OSRC2 cells were provided by ATCC. 786-O cells and OSRC-2 cells were maintained in RPMI Medium 1640 basic (Gibco; C11875500BT) supplemented with fetal bovine serum (FBS, 10 %, PAN; ST30–3302), penicillin–streptomycin–gentamicin (1 %, Solarbio; P1410), and cultured in 95 % air and 5 % CO2 at 37 °C.

Cell counting kit-8 (CCK-8) assay

Equal volumes of the cell suspension, containing 2000 cells per well, were aliquoted into 96-well plates, with three replicates per group. The plates were then placed in a cell incubator maintained at 37 °C with 5 % CO2. Following incubation periods of 24, 48, and 72 h within the incubator, 100 μl of the assay solution—comprising 80 μl of complete growth medium and 20 μl of CCK8 reagent—was added to each well. The plates were returned to the incubator for an additional 2 h.

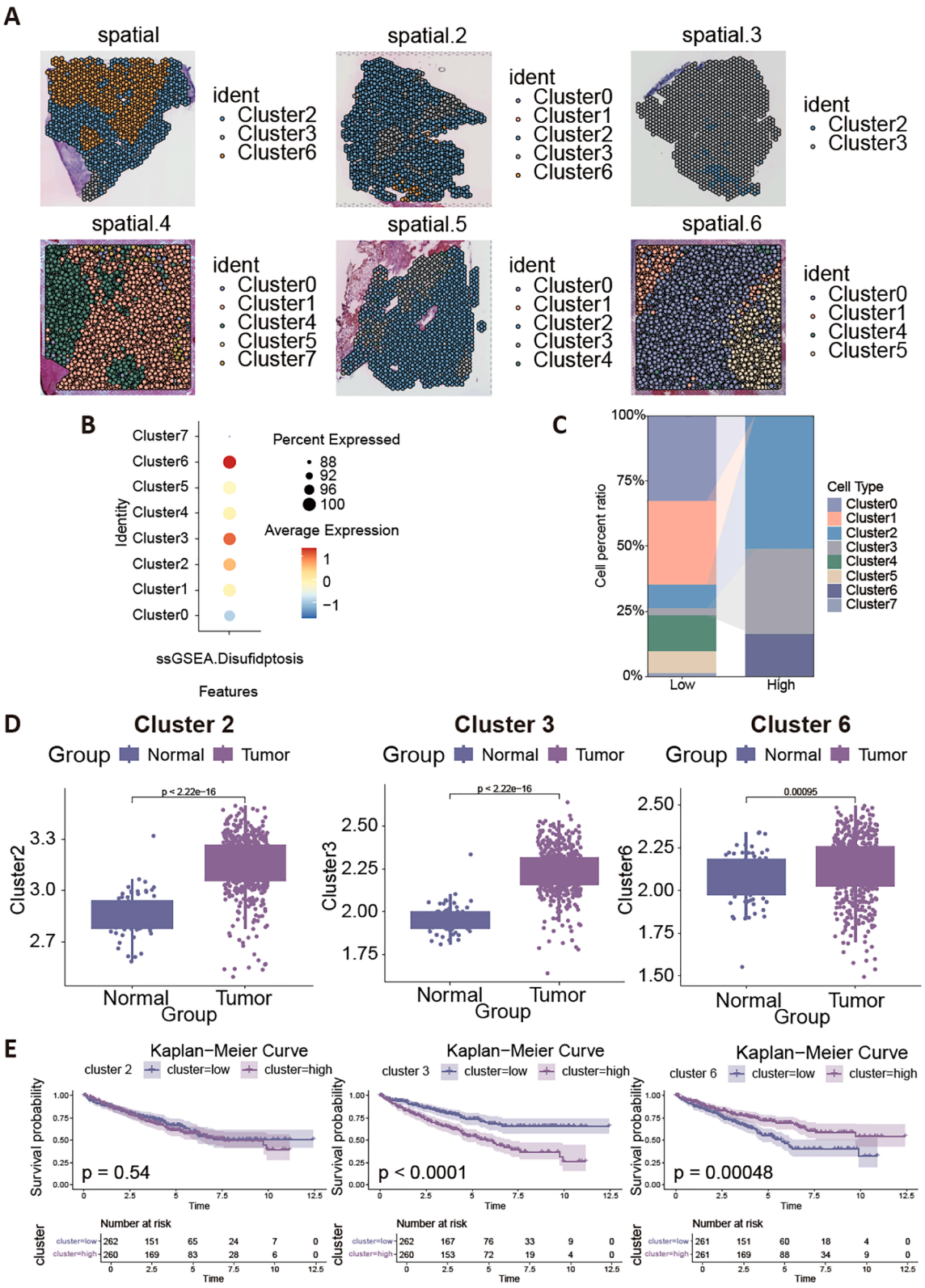

Fig. 1. Spatial transcriptomics reveals pronounced heterogeneity of disulfidptosis in renal cancer and localizes disulfidptosis-associated epithelial subpopulations. (A) Spatial spot layout and unsupervised clustering across six renal cancer sections, colored by cluster identities. (B) Dot plot showing the disulfidptosis scores across clusters. (C) Proportions of clusters within high- versus low-disulfidptosis groups defined by the section-specific median score. (D) Differential expression of cluster 2/3/6 signatures between tumor and adjacent tissues in TCGA-KIRC. (E) Kaplan–Meier survival analyses for cluster 2/3/6 signatures in TCGA-KIRC. Statistical significance was assessed by two-sided Wilcoxon rank-sum or Kruskal–Wallis tests with Benjamini–Hochberg FDR correction for group comparisons, Spearman's ρ for correlations, and log-rank tests for survival (hazard ratios estimated by Cox proportional hazards models), unless otherwise indicated.

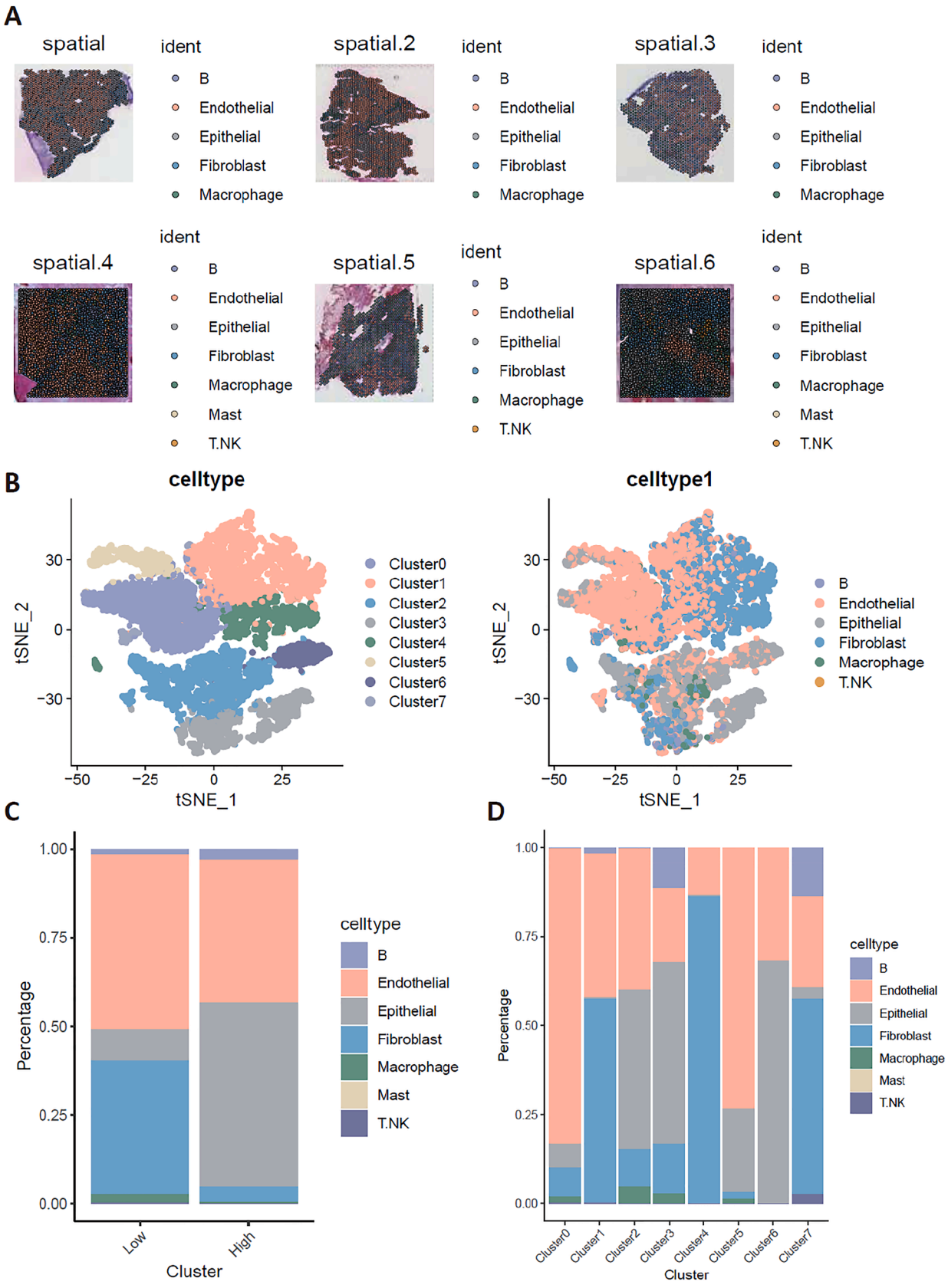

Fig. 2. Spatial deconvolution identifies epithelial-enriched disulfidptosis–associated cellular subpopulations. (A) Cell-type annotations across six spatial sections using RCTD, displayed on tissue coordinates. (B) t-SNE embeddings linking spatial clusters to deconvolved cell types. (C) Cell-type composition stratified by high versus low disulfidptosis score per section. (D) Cell-type composition of each spatial cluster, highlighting epithelial predominance in clusters 2, 3, and 6. Statistical comparisons of compositions were performed using two-sided Wilcoxon rank-sum tests on spot-level proportions or Fisher's exact tests on counts, with FDR correction.

Subsequently, absorbance at 450 nm was monitored at various time points using a microplate reader.

Wound healing assay

Cells of the 786O and OSRC2 lines, transfected to exhibit reduced PDLIM1 expression, were seeded into 6-well plates. Manual scratches were created within the cell monolayers, and the plates were then subjected to standard culture conditions for a duration of 24 h. To monitor the healing process of the scratches, photographs were captured at intervals of every 12 h.

Transwell assay

Post-centrifugation of the digested cell suspension, the supernatant was carefully aspirated, leaving behind the renal cell carcinoma (RCC) cells—786O and OSRC2. These cells were subsequently resuspended in a serum-free medium. A volume of 200 μl, containing approximately 1 × 10^5 cells, was then aliquoted into the upper compartment of a transwell chamber. Subsequently, the lower compartment was filled with 500 μl of culture medium supplemented with 20 % Fetal Bovine Serum (FBS). After a 24-hour incubation period under standard culture conditions, the migratory activity of the cells was assessed. The number of cells that had migrated to the selected area was enumerated using ImageJ software, a powerful tool for image analysis.

RCTD

We performed Robust Cell Type Decomposition (RCTD) using the scRNA-seq reference annotated at the major lineage and epithelial subcluster levels. Positive markers per cell type were obtained with Seurat::FindAllMarkers. RCTD was run in doublet mode to allow mixed spots, with cell size factors estimated per spot. We supplied UMI counts and gene-by-cell counts after intersecting gene symbols and filtering mitochondrial/ribosomal genes following RCTD recommendations. Cross-validation with SPOTlight and cell2location is described above; markers used by RCTD are provided in Supplementary Fig 3. We additionally performed spatial deconvolution with SPOTlight, which learns cell type–specific topic profiles from the scRNA-seq reference via non-negative matrix factorization and projects them onto Visium spots to estimate per-spot cell type proportions.

CytoTRACE

We inferred epithelial trajectories using Monocle2 on highly variable genes from tumor epithelial clusters, with the graph learned via UMAP embeddings (reduction_method="UMAP", use_partition=FALSE). Root states were anchored to proximal-tubule-like cells defined by canonical markers. Pseudotime was rescaled to [0,1]. Stemness was quantified with CytoTRACE using raw counts. Program activation (integrin-FAK axis, YAP/TAZ targets, ECM modules) was scored per cell (ssGSEA) and modeled along pseudotime using generalized additive models, with FDR-corrected smooth terms (Benjamini–Hochberg).

Statistical analyses

The statistical analyses conducted in this study utilized R version 4.0.2. For the quantitative data, variables that were normally distributed were assessed for statistical significance using Student's *t*-tests. In contrast, variables that did not follow a normal distribution were evaluated using the Wilcoxon rank-sum test. When it came to comparing more than two groups, nonparametric and parametric methods were employed, specifically the Kruskal-Wallis test and one-way analysis of variance (ANOVA), respectively. For the analysis of contingency tables, depending on the specific grouping conditions, the Chi-square test and Fisher's exact test were selected as appropriate statistical tools. To investigate the relationship between the metabolic transcriptomic pattern and patient prognosis, Kaplan-Meier survival analysis and the Cox proportional hazards model were engaged. These survival analyses were performed using the R package "Survminer" (version 0.4.6). All statistical comparisons were conducted as two-sided tests with a significance level (alpha) set at 0.05. To manage the false discovery rate (FDR) in the context of multiple hypothesis testing, the Benjamini-Hochberg method was applied. Normality was assessed by Shapiro–Wilk; variance homogeneity by Levene's test. For two-group comparisons we used two-sided Student's t-test (equal variances) or Welch's t-test (unequal), and Wilcoxon rank-sum for non-normal data. For >2 groups, one-way ANOVA with Tukey HSD or Kruskal–Wallis with Dunn's test (BH-adjusted) was used. Correlations used Spearman unless stated; 95 % CIs were obtained by 1000-fold bootstrap. Effect sizes (Cohen's d or Cliff's delta) and exact P/FDR values are reported in figure legends. Multiple testing was controlled with Benjamini–Hochberg within each analysis module.

Results

Result 1 Disulfidptosis exhibits marked intra- and inter-tumoral heterogeneity in renal cell carcinoma

We computed disulfidptosis scores using a curated gene set on six spatial transcriptomic sections from renal cancers (Fig. 1A). Disulfidptosis activity varies across sections. Unsupervised dimensionality reduction and clustering identified eight clusters with significant score differences; clusters 2, 3, and 6 displayed the highest disulfidptosis activity (Fig. 1B). When samples within each section were dichotomized at the section-specific median disulfidptosis score, clusters 2/3/6 were significantly enriched in the high-score group (Fig. 1C).

We then compared cluster 2/3/6 signature expression between tumor and matched adjacent tissues across five independent transcriptomic datasets (Fig. 1D, Supplementary Fig1). Clusters 2 and 3 were consistently higher in tumor versus adjacent tissue in KIRC, KIRP, GSE40435, GSE53757, and GSE167573. Cluster 6 was higher in tumor in KIRC but higher in adjacent tissue in the other cohorts, suggesting stronger tissue- or cohort-dependence for this cluster.

Survival analyses showed that higher expression of the cluster 3 signature was associated with worse outcomes; higher cluster 6 expression was likewise linked to poorer prognosis in TCGA-KIRC and TCGA-KIRP (Fig. 1E, Supplementary Fig2). Together, these data indicate pronounced spatial and cohort-level heterogeneity of disulfidptosis in renal cancer and highlight clusters 3 as key disulfidptosis-associated epithelial subpopulations with prognostic relevance.

Result 2 Disulfidptosis is most pronounced in epithelial cells, with key epithelial subclusters precisely localized

Using RCTD-based deconvolution, we annotated major lineages and epithelial subclusters across six spatial sections (Fig. 2A and B). In the high-disulfidptosis group, the epithelial fraction was significantly increased (Fig. 2C, left). Cluster 3 was predominantly epithelial (Fig. 2D), and clusters 2, 3, and 6—the clusters with elevated disulfidptosis activity—were each primarily composed of epithelial cells (Fig. 2B–D), indicating that epithelial compartments are the principal sites of disulfidptosis.

To evaluate robustness, we cross-deconvolved the same sections with SPOTlight. Per-lineage proportions from the two methods were positively associated overall, yet RCTD yielded higher and anatomically consistent epithelial estimates while down-weighting immune lineages that SPOTlight tended to inflate (Supplementary Fig3A-D). These results localize disulfidptosis most strongly to epithelial compartments and enable precise mapping of key epithelial subclusters.

Result 3. Single-cell integration maps disulfidptosis distribution in renal cell carcinoma

We integrated four renal cancer single-cell datasets (GSE131685, GSE207493, GSE159115, PRJNA768891). After quality control, the combined atlas comprised 30,974 cells from adjacent tissues and

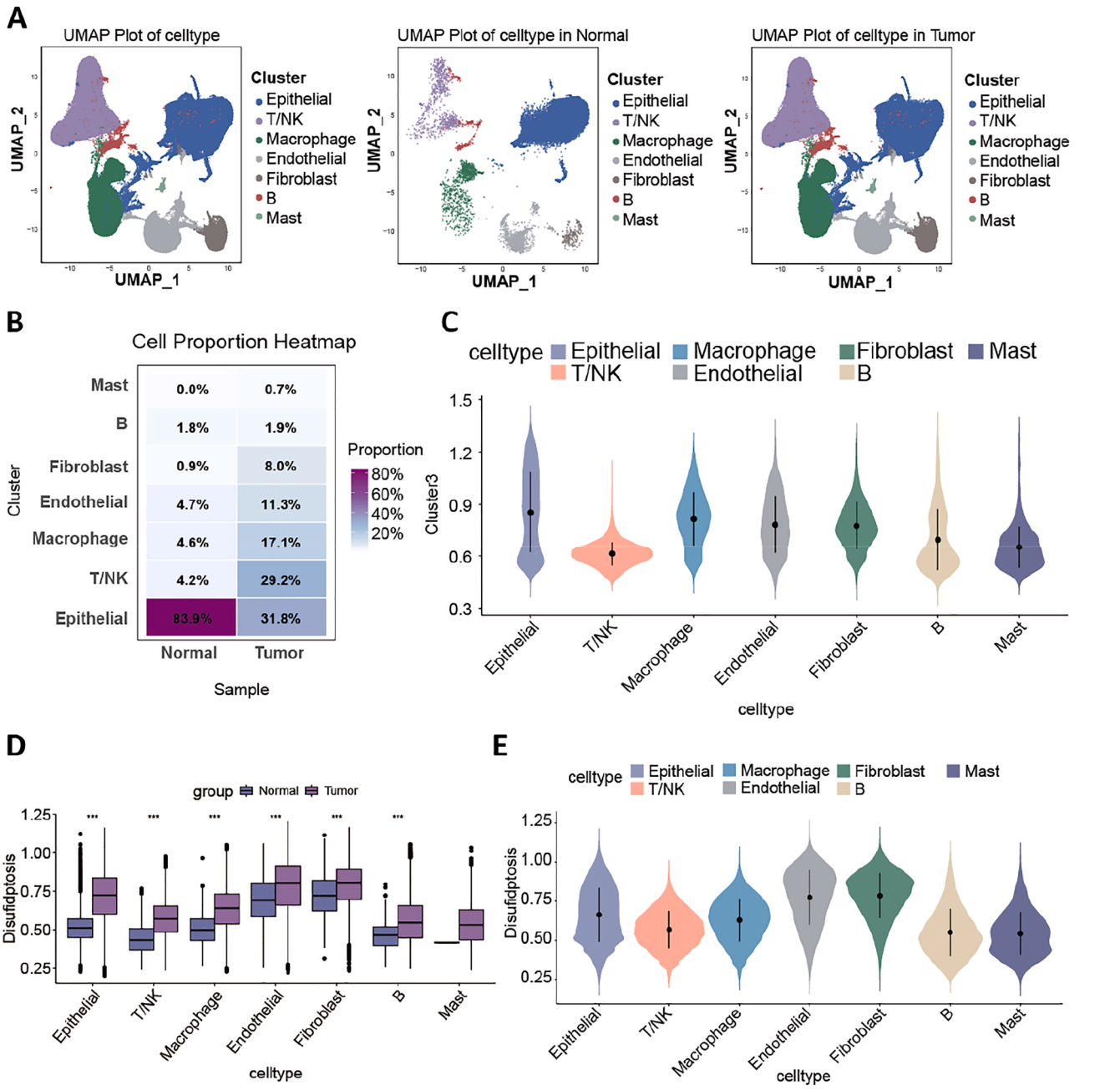

Fig. 3. Single-cell integration maps disulfidptosis distribution across cell types and tumor versus adjacent tissues. (A) UMAPs from integrated renal cancer scRNA-seq datasets, annotated by tumor versus adjacent status. (B) Bar plots of cell-type proportions at single-cell resolution in tumor and adjacent tissues. (C) Distribution of disulfidptosis scores across major cell types. (D) Within-cell-type comparisons of disulfidptosis scores between tumor and adjacent tissues. (E) Cluster-3 signature scores across cell types, showing enrichment in epithelial cells. Statistical significance was determined by Kruskal–Wallis tests with Dunn's post hoc comparisons (multi-group) and two-sided Wilcoxon rank-sum tests (two-group), with FDR correction.

192,131 cells from tumors (Fig. 3A and B). At single-cell resolution, disulfidptosis scores were higher in epithelial cells, endothelial cells, and fibroblasts (Fig. 3C). For most cell types, scores were elevated in tumor compared with adjacent tissues (Fig. 3D). Considering the prognostic association of the Cluster 3 signature (Results 1), we evaluated its distribution across cell types and observed prominent signals in epithelial cells alongside macrophages, endothelial cells, and fibroblasts (Fig. 3D and E). Considering effect sizes, differential expression patterns, and the absolute cell numbers represented, epithelial compartments emerge as a primary focus for downstream analyses.

Result 4. Epithelial reclustering pinpoints Epi_C5 as the key subcluster linked to disulfidptosis

After isolating epithelial cells and performing reclustering (Fig. 4A), epithelial subclusters showed distinct distributions between tumor and adjacent tissues: Epi_C1 and C0 were enriched in adjacent tissue, whereas C2–C6 were increased in tumors (Fig. 4B and C). Scoring each epithelial subcluster with the Cluster 3 signature and the disulfidptosis gene set (Fig. 4D and E) revealed that Epi_C5 achieved the highest scores on both metrics, indicating that Epi_C5 is the putative key epithelial subpopulation associated with disulfidptosis.

To determine where this program concentrates in tissue space, we projected per-spot Epi_C5 abundance, the disulfidptosis score, and the ECM program onto the Visium sections (Fig. 4F and G). Hotspots of Epi_C5 co-localized with disulfidptosis and showed concordant

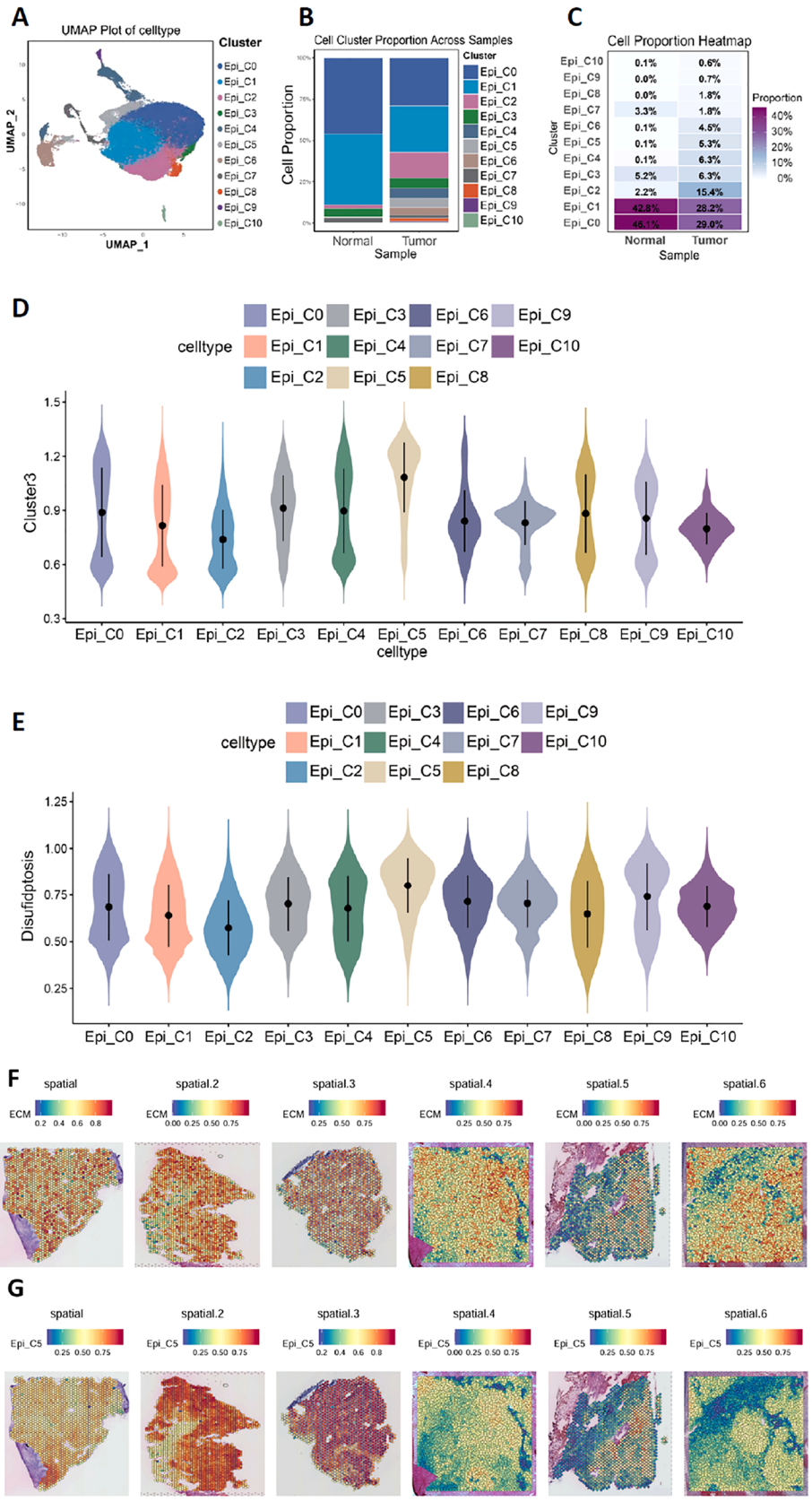

Fig. 4. Epithelial reclustering pinpoints Epi_C5 as the key subcluster linked to disulfidptosis. (A) Reclustering after isolating epithelial cells, shown on UMAP. (B) Absolute counts and (C) proportional composition of tumor versus adjacent epithelial cells across subclusters (B: counts; C: proportions). (D-E) Cluster-3 signature (D) and disulfidptosis scores (E) across epithelial subclusters, with Epi_C5 scoring highest on both metrics. (F) ECM scores across six spatial sections. (G) Epi_C5 scores across six spatial sections. Group comparisons used Kruskal–Wallis tests with Benjamini–Hochberg FDR correction; pairwise post hoc tests used Dunn's method.

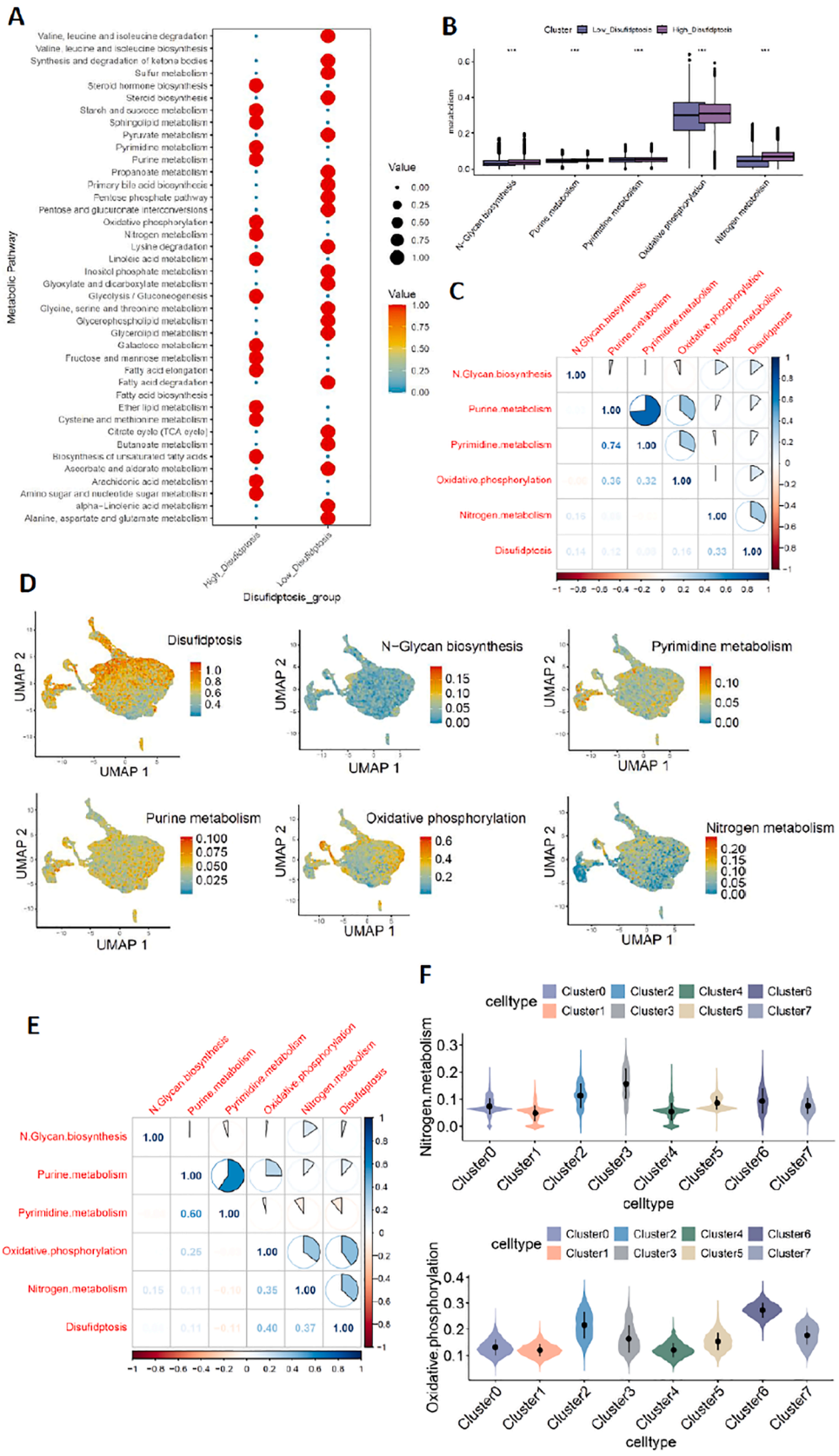

(caption on next page)

Fig. 5. Disulfidptosis co-occurs with upregulation of multiple metabolic pathways and shows spatially consistent patterns. (A) Dot plot of pathway enrichment (ssGSEA scores) comparing high versus low disulfidptosis groups at single-cell resolution (epithelial-focused). (B) Differential significance for five representative pathways (N-glycan biosynthesis, purine, pyrimidine, oxidative phosphorylation, nitrogen metabolism). (C) Summary of correlations between the five pathways and disulfidptosis scores. (D) Feature plots showing spatial distribution of the five pathways relative to disulfidptosis activity. (E) Summary of pathway–disulfidptosis correlations in spatial data. (F) Nitrogen metabolism (top) and oxidative phosphorylation (bottom) scores across spatial clusters, highlighting clusters 2/3/6. Statistical comparisons used two-sided Wilcoxon rank-sum or Kruskal–Wallis tests with FDR correction; correlations used Spearman's ρ with FDR adjustment for multiple testing.

elevation of ECM across sections. These patterns indicates that Epi_C5 marks epithelial neighborhoods with intensified disulfidptosis and matrix-remodeling activity.

Result 5. Disulfidptosis co-occurs with upregulation of multiple metabolic pathways and shows spatially consistent patterns

At the single-cell level, focusing on epithelial compartments, metabolic pathway analysis comparing high versus low disulfidptosis groups revealed significant enrichment of N-glycan biosynthesis, purine metabolism, pyrimidine metabolism, oxidative phosphorylation, and nitrogen metabolism in the high-score group (Fig. 5A and B, Supplementary Fig4). Correlation analyses indicated limited pairwise coupling among these five pathways (Fig. 5C). Feature plots demonstrated strong spatial overlap between regions of elevated nitrogen metabolism and areas with high disulfidptosis activity (Fig. 5D).

Repeating the analysis in spatial transcriptomic data yielded concordant results (Supplementary Fig4B-C). Moreover, when scoring clusters for nitrogen metabolism and oxidative phosphorylation, the disulfidptosis-high clusters (2, 3, and 6) ranked among the top for both pathways (Fig. 5F), supporting spatial co-localization between disulfidptosis activity and metabolic reprogramming.

Result 5. Disulfidptosis co-occurs with upregulation of multiple metabolic pathways and shows spatially consistent patterns

We next benchmarked the disulfidptosis score against ferroptosis, cuproptosis, oxidative stress, and cell-cycle programs, including a size-matched random gene set as a permutation control. Using per-cell Spearman correlations, disulfidptosis showed minimal coupling to ferroptosis, oxidative stress, cell cycle, and cuproptosis ($r \approx -0.24$ to 0.06), whereas ferroptosis and oxidative stress were strongly correlated and clustered together by hierarchical linkage (Supplementary Fig5). The random gene set exhibited only weak correlations with all programs, indicating that the decoupling is not driven by signature length or scoring artifacts. These data support that the disulfidptosis program is largely orthogonal to canonical oxidative-stress–driven death modalities and proliferative state, consistent with its spatial co-localization with ECM remodeling rather than global oxidative stress.

Result 6. Functional programs and clinical relevance of the disulfidptosis-associated epithelial subcluster

We first positioned epithelial subclusters along a common trajectory. Monocle2 revealed a branched manifold with a central bifurcation (nodes 1–2) giving rise to 3 p.m. (Supplementary Fig3E). Epi_C5 localized predominantly to the right-inferior branch downstream of node 2 (Supplementary Fig3F). Along this branch, EMT programs increased monotonically and peaked within the Epi_C5-enriched segment (Supplementary Fig3F-H); generalized additive models confirmed positive trends of EMT scores versus pseudotime within this arm. In contrast, the left arm showed comparatively lower EMT activity, consistent with more differentiated epithelial states.

To assess functional consequences, we contrasted epithelial cells with high versus low disulfidptosis scores. KEGG/GO analyses highlighted extracellular matrix organization, extracellular structure organization, ECM–receptor interaction, and ficolin-1–rich granule–related terms (Fig. 6A and B), reinforcing a matrix-remodeling and migratory/invasive program that aligns with the trajectory-based peaks.

Clinical relevance analyses using TCGA-KIRC and TCGA-KIRP showed that the Epi_C5 signature was significantly higher in tumors than in adjacent tissues, and higher expression associated with worse survival in both cohorts (Fig. 6C and D). CytoTRACE indicated that Epi_C5 occupies a more undifferentiated/stem-like state (Fig. 6E and F) and correlated positively with both the disulfidptosis score and the Cluster-3 signature (Fig. 6G), consistent with an intermediate-to-late, stress-adaptive epithelial program. Together, these data place Epi_C5 on a trajectory branch where ECM/mechanotransduction and EMT programs turn on, linking spatially anchored disulfidptosis to a stem-like, clinically adverse epithelial state.

Result 7. Intersection analysis prioritizes PDLIM1 as a candidate disulfidptosis-associated gene

To identify key genes linked to disulfidptosis in renal cancer, we intersected the disulfidptosis-related gene set with signature genes from Epi_C5 and Cluster 3, yielding PDLIM1 as a leading candidate (Fig. 7A). We next assessed PDLIM1 expression across multiple datasets (TCGA-KIRC, TCGA-KIRP, GSE40435, GSE53757, GSE167573) and observed consistently higher expression in tumors compared with adjacent tissues (Fig. 7B and D). Correlation analyses further showed that PDLIM1 expression positively associates with both the Cluster 3 and Epi_C5 signatures (Fig. 7C).

Stratifying cells by the median PDLIM1 expression, CytoTRACE scores were significantly higher in the PDLIM1-high group relative to the low group (Fig. 7E), indicating a more undifferentiated/stem-like state and suggesting greater malignant potential. Together, these findings support PDLIM1 as a disulfidptosis-associated candidate key gene meriting functional validation.

Result 8. PDLIM1 knockdown reduces proliferation, clonogenicity, and migration in renal cancer cells in vitro

To functionally evaluate PDLIM1, we performed shRNA-mediated knockdown in two renal cancer cell lines. qPCR confirmed robust reduction of PDLIM1 expression post-transfection (Fig. 8A). Relative to controls, PDLIM1 knockdown significantly decreased cell proliferation (Fig. 8B), impaired wound closure (Fig. 8C and D), and Transwell migration (Fig. 8E and F). Similar effects were reproduced with an independent siRNA. These results, consistent with multi-omic evidence, indicate that PDLIM1 promotes proliferative and migratory phenotypes in renal cancer cells, and that its depletion attenuates malignant behaviors.

Discussion

Since ccRCC exhibits pronounced intratumoral heterogeneity and stromal vascular patterning, combining single-cell resolution of cellular states with spatial restoration of tissue architecture is essential to localize pathway activity and infer niche-level interactions. By integrating spatial transcriptomics with multi-cohort single-cell RNA-seq, we chart the intratumoral organization of disulfidptosis-associated states in clear cell renal cell carcinoma (ccRCC) and localize their strongest signals to a tumor-epithelial subpopulation, Epi_C5. Beyond bulk-level risk scores, we anchor disulfidptosis to discrete cellular states and anatomical niches, translating a mechanistic concept into histologically resolved tumor phenotypes. Building on foundational studies, disulfidptosis can arise under restricted glucose uptake with perturbed thiol–disulfide homeostasis, leading to aberrant disulfide bonding in actin cytoskeletal proteins and F-actin collapse; pharmacologic inhibition of glucose transporters can elicit this program in susceptible models. Our data extend this framework by showing, in human tumors, where disulfidptosis-associated activity concentrates and which epithelial state is most involved, highlighting Epi_C5 as a putative tumor epithelial compartment where disulfidptosis transcriptional activity, stemness features, and extracellular-matrix programs converge.

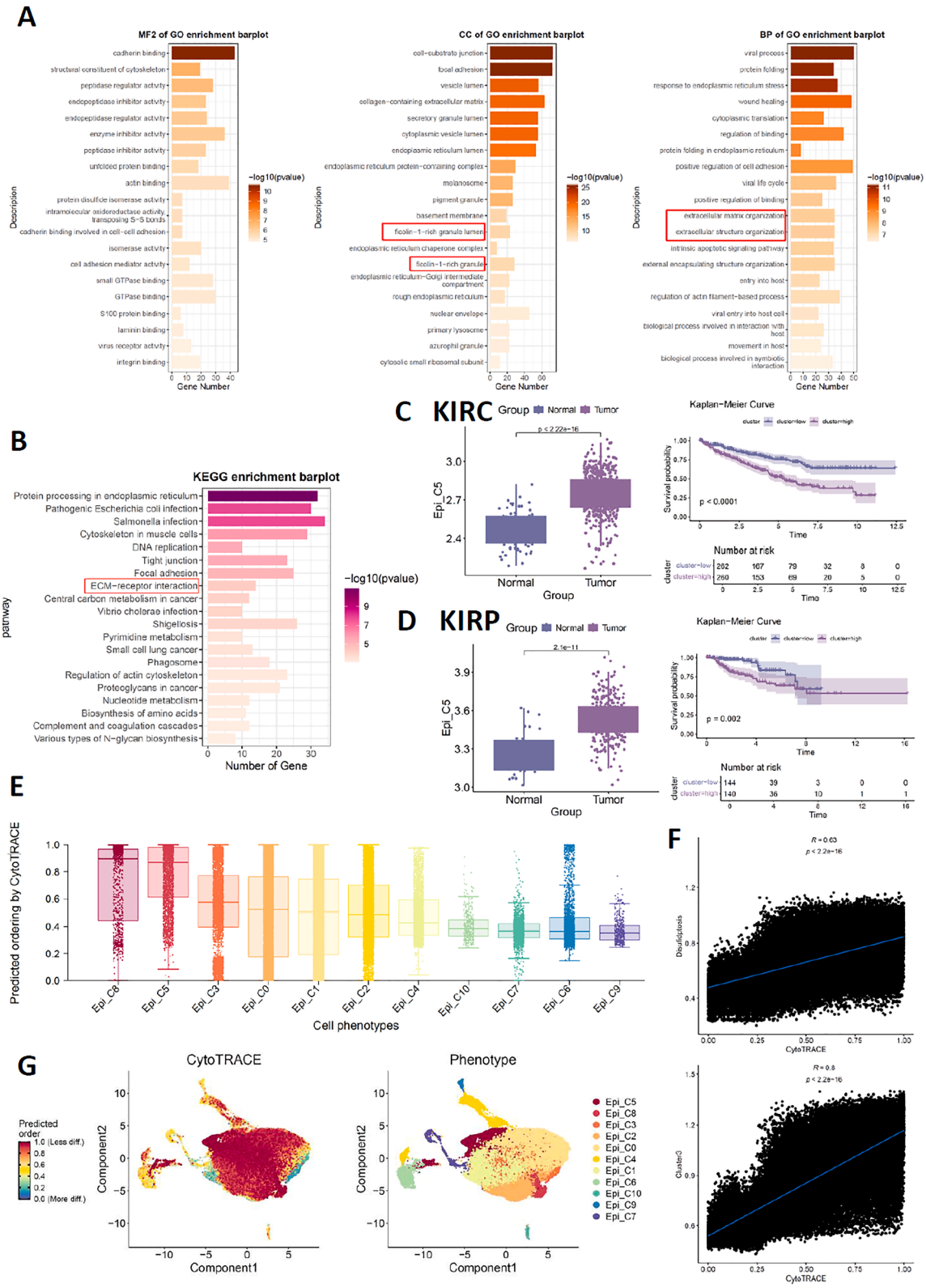

Fig. 6. Functional programs and clinical relevance of the disulfidptosis-associated epithelial subcluster. (A-B) KEGG (A) and GO (B) enrichment analyses comparing high versus low disulfidptosis epithelial cells, highlighting ECM/extracellular-structure programs. (C-D) Epi_C5 signature expression in tumor versus adjacent tissues and Kaplan–Meier survival analyses in TCGA-KIRC (C) and TCGA-KIRP (D). (E) CytoTRACE differentiation-potential scores across epithelial subclusters. (F) Correlations between CytoTRACE and disulfidptosis and Cluster-3 signature scores. (G) CytoTRACE differentiation-potential distribution. Group differences were tested with two-sided Wilcoxon rank-sum or Kruskal–Wallis tests (FDR-adjusted), correlations with Spearman's ρ (FDR-adjusted), and survival with log-rank tests and Cox models (reporting HR and 95 % CI).

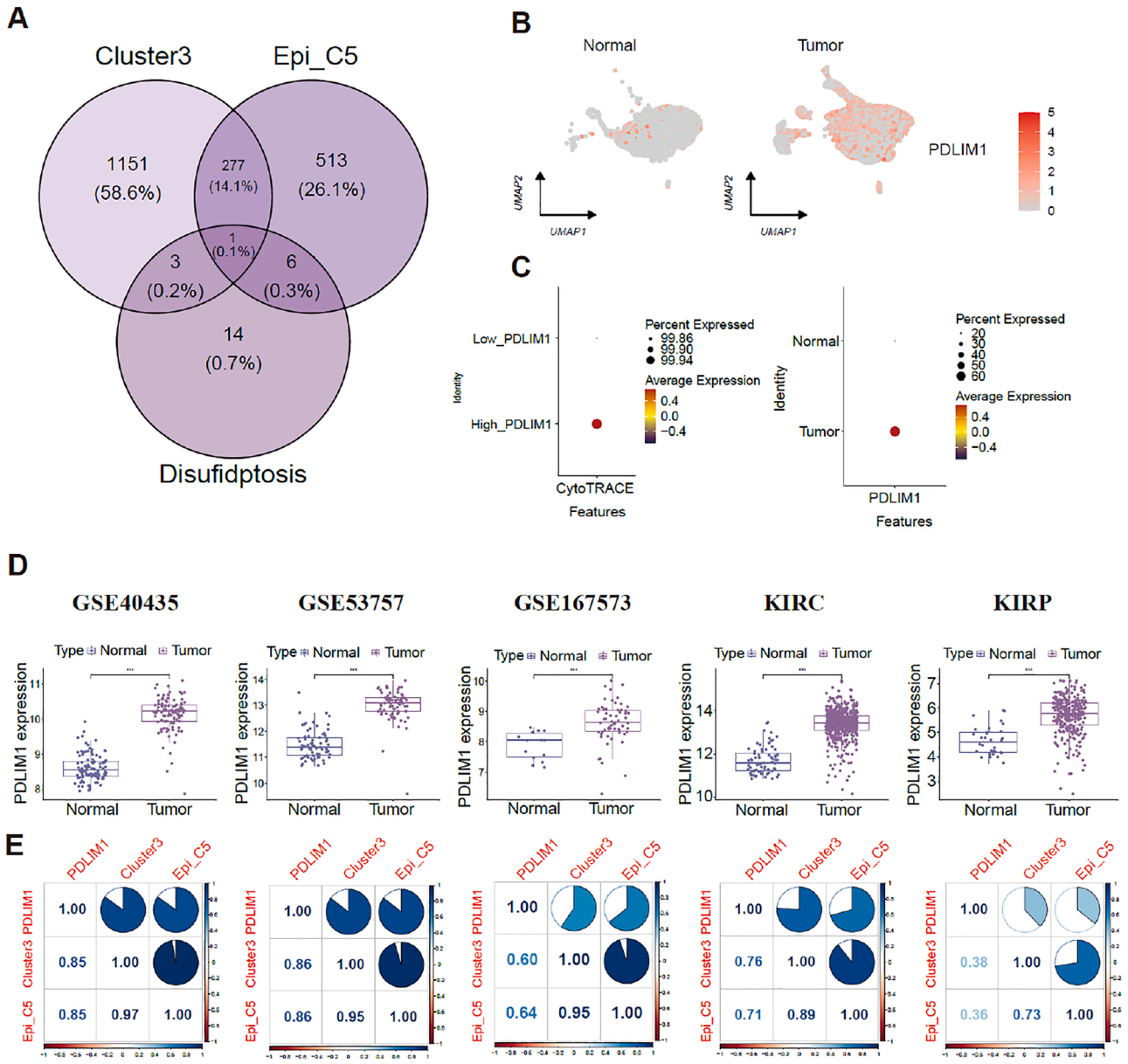

Fig. 7. Intersection analysis prioritizes PDLIM1 as a candidate disulfidptosis-associated gene. (A) Venn diagram showing intersection of the disulfidptosis gene set with Epi_C5 and Cluster-3 signature genes, nominating PDLIM1. (B) UMAP visualization of PDLIM1 expression in tumor versus adjacent single cells. (C) CytoTRACE analysis stratified by PDLIM1 expression (high vs. low). (D) PDLIM1 expression across renal cancer datasets (TCGA-KIRC, TCGA-KIRP, GSE40435, GSE53757, GSE167573), tumor versus adjacent. (E) Correlations between PDLIM1 and Cluster-3/Epi_C5 signatures. Statistical tests included two-sided Wilcoxon rank-sum (tumor vs. adjacent), Spearman's ρ (correlations), and log-rank/Cox models (survival), with Benjamini–Hochberg FDR correction where applicable.

From a spatial ecology perspective, regions with high disulfidptosis signatures co-localize with elevated oxidative phosphorylation, nitrogen and nucleotide metabolism, and enrichment of N-glycan biosynthesis, together with extracellular-matrix remodeling and adhesion-assembly programs. These domains are populated by epithelial cells with higher CytoTRACE-inferred immaturity and exhibit reinforced mechanotransduction. This refines classic center–periphery models of ccRCC by showing that metabolic flux, glycosylation, and ECM/adhesion programs concentrate in the same tissue territories and align with a distinct tumor epithelial state. Although macrophage, endothelial, and fibroblast lineages also show elevated disulfidptosis scores at single-cell resolution, epithelial compartments contribute the largest and most consistently localized share of signature-high cells, helping explain tissue-scale metabolic plasticity and heterogeneity in prognosis.

Trajectory analyses position Epi_C5 along a proximal-tubule–like to be dedifferentiated continuum with increasing stemness and progressive activation of ECM and mechanotransduction programs. Our data support a metabolism–redox–cytoskeleton coupling in which elevated oxidative phosphorylation and nucleotide synthesis increase reactive oxygen species while glucose limitation constrains NADPH/GSH buffering, creating a permissive window for actin disulfide stress. Under high adhesion tension, integrin–FAK–Src–RhoA–ROCK–LIMK signaling sustains stress fibers and raises the energetic and redox demand on actin maintenance, heightening susceptibility to disulfidptosis. Co-enrichment of YAP/TAZ target programs and FAK-axis signaling in Epi_C5-rich regions aligns with a feed-forward mechanotransduction loop: increased stiffness and integrin clustering promote YAP/TAZ nuclear localization, reinforcing cytoskeletal and ECM transcription and further stiffening the microenvironment. Consistent with a non-monotonic relationship between reactive species and cell death, these features delineate a permissive window in which OXPHOS and nucleotide biosynthesis,

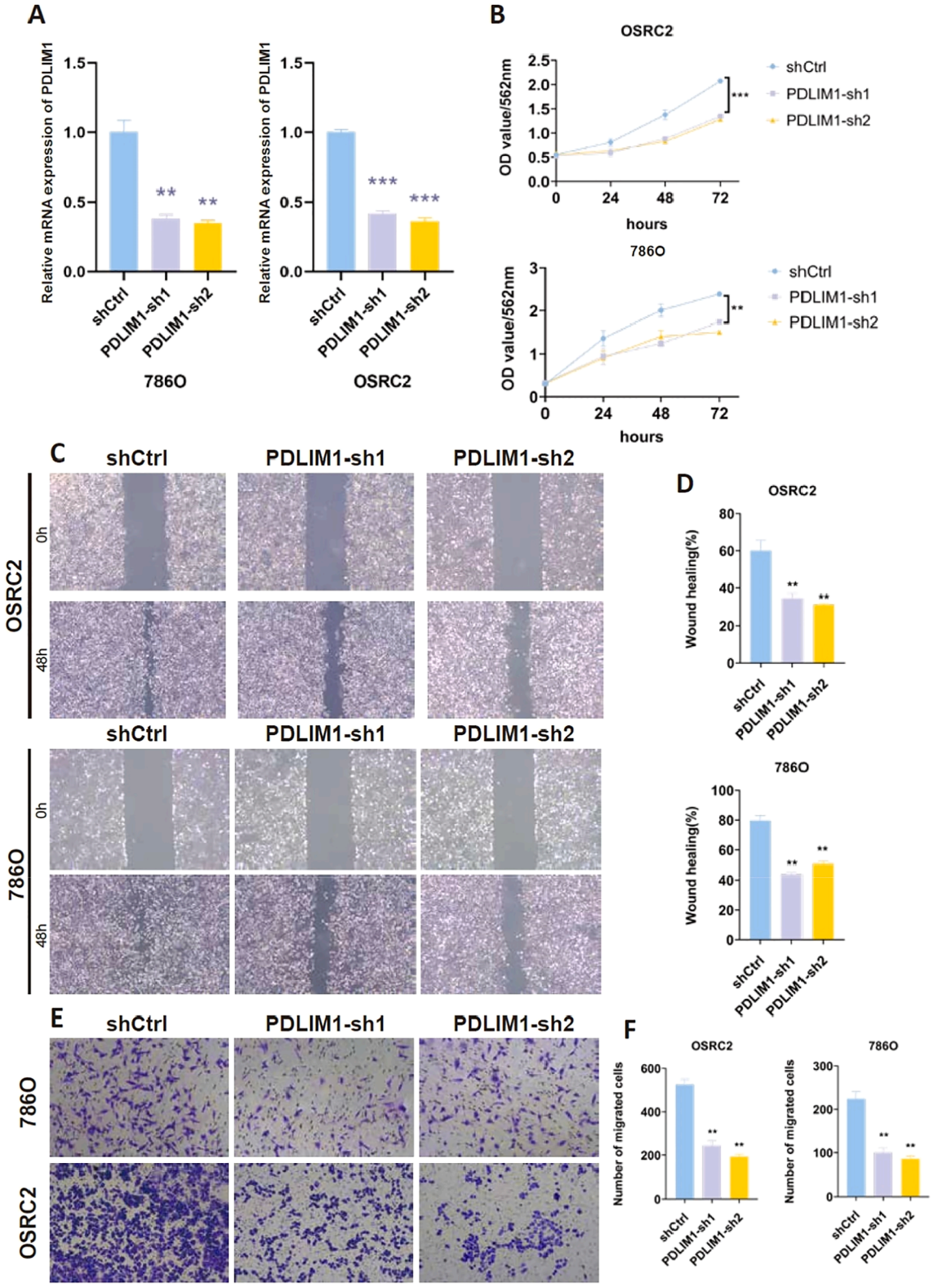

Fig. 8. PDLIM1 knockdown reduces proliferation, clonogenicity, and migration in renal cancer cells in vitro. (A) qPCR validation of siRNA/shRNA-mediated PDLIM1 knockdown in renal cancer cell lines (786-O and OSRC-2). (B) CCK-8 proliferation/viability curves comparing control and PDLIM1-depleted cells over time. (C-D) Representative images (C) and quantification (D) of wound-healing assays. (E) Transwell migration assays showing decreased motility/invasiveness after PDLIM1 depletion. (F) Quantification of transwell migration assays. Data are presented as mean ± SEM; statistical significance was determined by two-sided Student's t-test (two groups) or one-way ANOVA with Tukey's post hoc test (multiple groups), unless otherwise specified. ns, not significant; * FDR < 0.05; ** FDR < 0.01; *** FDR < 0.001.

together with rewired N-glycosylation and O-GlcNAcylation, bias integrin–FAK complex assembly and YAP/TAZ-dependent mechano-transcription to favor cytoskeletal/adhesion reconfiguration without necessarily committing to irreversible death. Functionally, this coupling promotes stress-fiber maintenance, adhesion turnover, and matrix remodeling, sustaining a partially EMT-like, stemness-high Epi_C5 state. Specificity is supported by a correlation heatmap contrasting the disulfidptosis score with ferroptosis, cuproptosis, oxidative-stress, and cell-cycle signatures, alongside size-matched random gene-set permutations (Supplementary Fig5).

Epi_C5 is transcriptionally distinct from other epithelial subsets by concurrent enrichment of disulfidptosis, stemness, and ECM/mechanotransduction programs. While adjacent subsets share proximal-tubule features, Epi_C5 uniquely co-expresses adhesion and cytoskeletal modules and concentrates at tumor–stroma interfaces, suggesting a niche-adapted malignant state rather than a purely lineage-defined population.

In RCC cells, PDLIM1 exhibits predominant cytoplasmic localization with enrichment along stress fibers and focal-adhesion–adjacent puncta, consistent with its role as a PDZ–LIM scaffold linking α-actinin and actin to adhesion complexes. Functionally, this position enables coupling of integrin–FAK signaling to cytoskeletal organization and Hippo pathway activity, providing a plausible conduit through which redox–cytoskeletal stress influences mechanotransduction. Across cancer types, PDLIM1 is recurrently linked to cytoskeletal remodeling, adhesion signaling [32], and increased invasive potential [38]. It is upregulated in diffuse large B-cell lymphoma [39], where its inhibition curtails proliferation and induces apoptosis; its reduction accompanies drug-induced apoptosis in esophageal squamous cell carcinoma; prognostic models in glioblastoma include PDLIM1 as a risk contributor [40]; studies of hepatocellular carcinoma drug resistance place PDLIM1 within a disulfidptosis-associated cytoskeletal module [33]; and in liver fibrosis, PDLIM1 promotes hepatic stellate cell activation and amplifies TGF-β signaling [41], reinforcing ECM remodeling and mechanobiology. In our spatial and single-cell ccRCC data, PDLIM1 is enriched in the Epi_C5 state and co-localizes with FAK-axis signaling and YAP/TAZ target programs [42]. These functions nominate PDLIM1 as an actin–adhesion scaffold that links ECM organization to FAK/Src and YAP/TAZ-dependent mechanotransduction in ccRCC. Given potential tissue-context dependencies, ccRCC-specific in vivo validation using domain-focused perturbations with orthogonal readouts (pFAK, nuclear YAP, focal-adhesion turnover, ECM deposition) is a priority.

Important limitations warrant emphasis. First, pathway activities were largely inferred from gene-set scores rather than direct functional readouts and may be partially collinear with proliferation or generalized oxidative stress. Second, multi-source cohorts inevitably introduce batch and sampling variability; notably, the directionality of one cluster varied by cohort, hinting at influences from stromal composition, microvascular density, hypoxia–reoxygenation dynamics, and histologic context. Most critically, our functional validations are restricted to cell lines and lack in vivo causality. To bridge this gap, we propose three lines of investigation. First, orthotopic (renal cortex or subcapsular) and patient-derived SLC7A11-high xenografts with PDLIM1 knockdown or overexpression to assess in situ growth, local invasion, and distant metastasis, coupled with tissue-level pharmacodynamic endpoints. Second, induction of disulfidptosis with GLUT1/3 inhibitors combined with FAK inhibitors or Src inhibitors to test a dual-modality strategy that drives cells toward the disulfidptosis threshold while dampening mechanoadaptation, with concurrent evaluation of tumor control and toxicity. Third, we will apply spatial proteomics and metabolomics to delineate immune exclusion and mechanical barriers in Epi_C5-rich regions and to link these features to immunotherapy response.

Clinically, a composite panel integrating an Epi_C5 score with markers of mechanotransduction and redox–cytoskeletal coupling could stratify tumors with high disulfidptosis-associated activity. The spatial concentration of these programs at fibrovascular interfaces suggests combination strategies pairing glucose-uptake inhibition with focal-adhesion or Src-family kinase blockade.

In summary, we propose a spatial–cellular model spanning metabolism, redox, cytoskeleton, and matrix: Within specific microenvironments, metabolic reprogramming and redox imbalance induce disulfidptosis-related states; PDLIM1 and allied scaffolds translate stress signals into mechanoadaptive programs and ECM remodeling, shaping a stemness-high, invasive epithelial subpopulation. This framework reconciles intratumoral spatial heterogeneity with prognostic divergence and nominates a testable therapeutic avenue combining metabolic limitation with mechanotransduction blockade. The next step is rigorous in vivo causal validation in orthotopic and patient-derived models, alongside evaluation of combination regimens and biomarker-guided patient selection. These findings provide a spatially grounded rationale to co-target redox–cytoskeletal vulnerabilities and mechanotransduction in a biomarker-defined subset of RCC.

Funding statement

This study is supported by Shanghai Province Zhong Zhi Zhong Project (2022ZZ01011) and National Natural Science Foundation of China (82072825, 81772740, 82173345, 8197233, 82372883, 81874093, 2022YFB4700904), ChangFeng Talent Development Project (grant numbers: 2023CF001), Shanghai Anticancer Association EYAS Project (grant numbers: SACA-CY25C01).

Data availability

All data analyzed in this study are publicly available. Spatial transcriptomics data were retrieved from GEO under accession GSE175540 (six sections). Public single-cell RNA-seq references were obtained from GEO under accessions GSE156632 and GSE144735. Bulk RNA-seq profiles, matched clinical annotations, and somatic mutation calls for TCGA Kidney Clear Cell Carcinoma (KIRC) and Kidney Papillary Cell Carcinoma (KIRP) were downloaded from the NCI Genomic Data Commons (TCGA projects KIRC and KIRP). External validation datasets with clinical annotations were obtained from GEO under accessions GSE167573, GSE40435, and GSE53757.

Ethics approval

The procedure related to human subjects was approved by the Ethics Committee of the Changhai Hospital (No. CHEC2024–058).

CRediT authorship contribution statement

Wenqiang Liu: Writing – original draft. **Xianglin Liu:** Methodology. **Juan Yi:** Resources. **Zhao Tang:** Data curation. **Ziwen Dai:** Validation. **Jiaao Song:** Methodology. **Tong Chen:** Methodology. **Jun Wang:** Methodology. **Jiaxuan Wang:** Resources. **Wentao Jiang:** Resources. **Aimin Jiang:** Software. **Zhenjie Wu:** Supervision. **Lifang Tang:** Validation. **Yuming Jin:** Methodology. **Yinghu Chen:** Validation. **Linhui Wang:** Conceptualization.

Declaration of competing interest

The authors declare that they have no known competing financial interests or personal relationships that could have appeared to influence the work reported in this paper.

Acknowledgements

Not applicable.

Supplementary materials

Supplementary material associated with this article can be found, in the online version, at doi:10.1016/j.tranon.2026.102765.

References

[1] M.T. Alamsyah, F.F. Prapiska, S.M. Warli, The impact of deferred cytoreductive nephrectomy on survival in advanced renal cell carcinoma: a systematic review and meta-analysis, Asian J. Urol. 12 (2) (2025) 204–209, https://doi.org/10.1016/j.ajur.2024.06.003.

[2] B. Han, R. Zheng, H. Zeng, S. Wang, K. Sun, R. Chen, J. He, Cancer incidence and mortality in China, 2022, J. Natl. Cancer Cent. 4 (1) (2024) 47–53, https://doi.org/10.1016/j.jncc.2024.01.006.

[3] A. Jiang, J. Li, Z. He, Y. Liu, K. Qiao, Y. Fang, L. Wang, Renal cancer: signaling pathways and advances in targeted therapies, MedComm. (2020) 5 (8) (2024) e676, https://doi.org/10.1002/mco2.676.

[4] H. Bolek, E. Sertesen Camoz, O.F. Kuzu, H. Karakas, S. Sim, S. Sekmek, Y. Urun, Prognostic role of smoking in metastatic renal cell carcinoma in real-world data from the Turkish Oncology Group Kidney Cancer Consortium (TKCC), Sci. Rep. (2026), https://doi.org/10.1038/s41598-026-35435-3.

[5] A.A. Grosso, V. Salamone, F. Di Maida, S. Giudici, A. Cadenar, L. Lambertini, A. Minervini, Robot-assisted partial nephrectomy for renal cell carcinoma: a narrative review of different clinical scenarios, Asian J. Urol. 12 (2) (2025) 210–216, https://doi.org/10.1016/j.ajur.2024.09.010.

[6] H. Sung, J. Ferlay, R.L. Siegel, M. Laversanne, I. Soerjomataram, A. Jemal, F. Bray, Global Cancer statistics 2020: GLOBOCAN estimates of incidence and mortality worldwide for 36 cancers in 185 countries, CA Cancer J. Clin. 71 (3) (2021) 209–249, https://doi.org/10.3322/caac.21660.

[7] X. Wang, J. Li, Y. Zhang, R. Huang, P. Zhang, H. Hu, Ferroptosis in renal cell carcinoma: integrative multi-omics insights and therapeutic perspectives, Int. J. Surg. (2026), https://doi.org/10.1097/JS9.0000000000004583.

[8] J. Zhang, J. Gu, R. Xia, J. Yin, X. Wang, J. Yang, S. Guo, A promising magnesium-related alloy with metabolic reprogramming and antitumor effects in hepatocellular and pancreatic cancer, Bioact. Mater. 59 (2026) 186–204, https://doi.org/10.1016/j.bioactmat.2025.12.039.

[9] K. Attalla, R.G. DiNatale, P.M. Rappold, C.J. Fong, F. Sanchez-Vega, A.W. Silagy, A. A. Hakimi, Prevalence and landscape of actionable genomic alterations in renal cell carcinoma, Clin. Cancer Res. 27 (20) (2021) 5595–5606, https://doi.org/10.1158/1078-0432.CCR-20-4058.

[10] J.E. Chan, T. Tammela, Decoding subclonal anti-tumor immunity, Cancer Cell 43 (10) (2025) 1783–1785, https://doi.org/10.1016/j.ccell.2025.06.018.

[11] A. Fernandez-Sanroman, A. Fendler, B.J.Y. Tan, A.L. Cattin, C. Spencer, R. Thompson, S. Turajlic, Tracking nongenetic evolution from primary to metastatic ccRCC: tRACERx renal, Cancer Discov. (2025) OF1–OF23, https://doi.org/10.1158/2159-8290.CD-24-0499.

[12] A. Jiang, J. Meng, W. Gong, Z. Zhang, X. Gan, J. Wang, L. Wang, Elevated SNRPA1, as a promising predictor reflecting severe clinical outcome via effecting tumor immunity for ccRCC, is related to cell invasion, metastasis, and sunitinib sensitivity, Front. Immunol. 13 (2022) 842069, https://doi.org/10.3389/fimmu.2022.842069.

[13] G.B.D.L.R. Infections, Antimicrobial Resistance, C., Global burden of lower respiratory infections and aetiologies, 1990-2023: a systematic analysis for the global burden of disease study 2023, Lancet Infect. Dis. (2025), https://doi.org/10.1016/S1473-3099 (25)00689-9.

[14] T. Jin, J. Ma, L. Wang, X. Liu, M. Wu, B. Wang, Q. He, PTPN22 dephosphorylates CBL to inhibit PD-L1 ubiquitination and drive immunosuppression in renal cell carcinoma, Int. J. Biol. Sci. 22 (2) (2026) 663–683, https://doi.org/10.7150/ijbs.122418.

[15] Z.T. Aimin Jiang, Hanzhong Zhang, Jinxin Li, Jialin Meng, Ying Liu, Yu Fang, Juan Lu, Xu Zhang, Le Qu, Anqi Lin, Linhui Wang, Current application status and innovative development of surgical robot, Med. Res. 1 (3) (2025) 378–396, https://doi.org/10.1002/mdr2.70014.

[16] S. Govindu, P. Gowda, M. Muquith, M. Espinoza, D. Hsiehchen, Primary and secondary pseudo-stability and progression after atezolizumab with and without bevacizumab, J. ImmunOther Cancer 14 (1) (2026), https://doi.org/10.1136/jitc-2025-013727.

[17] B. Gan, Redox-driven cell death by disulfidptosis and its therapeutic potential, Nat. Rev. Mol. Cell Biol. 26 (10) (2025) 727–729, https://doi.org/10.1038/s41580-025-00888-3.

[18] C. Mao, D. Jiang, A.C. Koong, B. Gan, Exploiting metabolic cell death for cancer therapy, Nat. Rev. Cancer 26 (1) (2026) 27–45, https://doi.org/10.1038/s41568-025-00879-8.

[19] A. Jiang, W. Liu, Y. Liu, J. Hu, B. Zhu, Y. Fang, L. Wang, DCS, a novel classifier system based on disulfidptosis reveals tumor microenvironment heterogeneity and guides frontline therapy for clear cell renal carcinoma, J. Natl. Cancer Cent. 4 (3) (2024) 263–279, https://doi.org/10.1016/j.jncc.2024.06.003.

[20] J. Wan, J.H. Shi, M. Shi, H. Huang, Z. Zhang, W. Li, Q. Zou, Lactate dehydrogenase B facilitates disulfidptosis and exhaustion of tumour-infiltrating CD8 (+) T cells, Nat. Cell Biol. 27 (6) (2025) 972–982, https://doi.org/10.1038/s41556-025-01673-2.

[21] M. Zhang, H. Zheng, H. Jin, X. Zhu, S. Liu, Y. Chen, S. Zhang, Regulating SLC7A11/GSH/GPX4 axis by glucose dyshomeostasis to simultaneously promote disulfidptosis, cuproptosis and ferroptosis, Bioact. Mater. 54 (2025) 744–758, https://doi.org/10.1016/j.bioactmat.2025.09.003.

[22] X. Liu, L. Nie, Y. Zhang, Y. Yan, C. Wang, M. Colic, B. Gan, Actin cytoskeleton vulnerability to disulfide stress mediates disulfidptosis, Nat. Cell Biol. 25 (3) (2023) 404–414, https://doi.org/10.1038/s41556-023-01091-2.

[23] H.F. Yao, J. Ge, J. Chen, X. Tang, C. Li, X. Hu, C. Jiang, CASC8 activates the pentose phosphate pathway to inhibit disulfidptosis in pancreatic ductal adenocarcinoma though the c-myc-GLUT1 axis, J. Exp. Clin. Cancer Res. 44 (1) (2025) 26, https://doi.org/10.1186/s13046-025-03295-w.

[24] C. Chen, M. An, H. Zheng, M. Pang, Y. Li, X. Diao, T. Lin, B cells disrupt tertiary lymphoid structure formation and suppress anti-tumor immunity, Cancer Cell (2026), https://doi.org/10.1016/j.ccell.2025.12.011.

[25] A. Jiang, Y. Liu, Z. He, W. Liu, Q. Yang, Y. Fang, L. Wang, TDERS, an exosome RNA-derived signature predicts prognosis and immunotherapeutic response in clear cell renal cell cancer: a multicohort study, J. Natl. Cancer Cent. 4 (4) (2024) 382–394, https://doi.org/10.1016/j.jncc.2024.07.002.

[26] V. Marteau, N. Nemati, K. Handler, D. Raju, A. Kirchmair, D. Rieder, Z. Trajanoski, Single-cell integration and multi-modal profiling reveals phenotypes and spatial organization of neutrophils in colorectal cancer, Cancer Cell 44 (1) (2026) 146–165, https://doi.org/10.1016/j.ccell.2025.12.003, e114.

[27] A. Enninful, Z. Zhang, D. Klymyshyn, M. Ingalls, M. Yang, H. Zong, R. Fan, Integration of imaging-based and sequencing-based spatial omics mapping on the same tissue section via DBiTplus, Nat. Methods (2026), https://doi.org/10.1038/s41592-025-02948-0.

[28] Y. Hu, L. Wu, S. Qu, W.T. Kong, X. Yu, J. Xu, S. Chakarov, Temporal and spatial atlas of eosinophil specialization across tissues, Nat. Immunol. (2026), https://doi.org/10.1038/s41590-025-02382-6.

[29] F. Ji, H. Chen, H. Li, J. Zhang, S. Li, P. Wang, J. Dong, A subcellular spatial atlas illuminates the microenvironmental remodeling of perineural invasion in distal cholangiocarcinoma, J. Hematol. Oncol. 19 (1) (2026) 6, https://doi.org/10.1186/s13045-025-01773-4.

[30] G.S. Gulati, J.P. D'Silva, Y. Liu, L. Wang, A.M Newman, Profiling cell identity and tissue architecture with single-cell and spatial transcriptomics, Nat. Rev. Mol. Cell Biol. 26 (1) (2025) 11–31, https://doi.org/10.1038/s41580-024-00768-2.

[31] M. Kang, G.S. Gulati, E.L. Brown, Z. Qi, S. Avagyan, J.J.A. Armenteros, A. M. Newman, Improved reconstruction of single-cell developmental potential with CytoTRACE 2, Nat. Methods 22 (11) (2025) 2258–2263, https://doi.org/10.1038/s41592-025-02857-2.

[32] H.N. Chen, K. Yuan, N. Xie, K. Wang, Z. Huang, Y. Chen, C. Huang, PDLIM1 stabilizes the E-cadherin/beta-catenin complex to prevent epithelial-mesenchymal transition and metastatic potential of colorectal cancer cells, Cancer Res. 76 (5) (2016) 1122–1134, https://doi.org/10.1158/0008-5472.CAN-15-1962.

[33] Z. Huang, J.K. Zhou, K. Wang, H. Chen, S. Qin, J. Liu, Y. Peng, PDLIM1 Inhibits tumor metastasis through activating hippo signaling in hepatocellular carcinoma, Hepatology 71 (5) (2020) 1643–1659, https://doi.org/10.1002/hep.30930.

[34] C. Qiu, Y. Duan, B. Wang, J. Shi, P. Wang, H. Ye, X. Wang, Serum anti-PDLIM1 autoantibody as diagnostic marker in ovarian cancer, Front. Immunol. 12 (2021) 698312, https://doi.org/10.3389/fimmu.2021.698312.

[35] X. Shen, Y. Zhao, Y. Cao, Y. Liu, J. Ruan, C. Wang, G. Zhu, Identification of PDLIM1 as a glioblastoma stem cell marker driving tumorigenesis and chemoresistance, Cell Death. Discov. 10 (1) (2024) 469, https://doi.org/10.1038/s41420-024-02241-7.

[36] M. Kim, M. Zheng, S.Z. Tian, B. Lee, J.H. Chuang, Y. Ruan, MIA-sig: multiplex chromatin interaction analysis by signal processing and statistical algorithms, Genome Biol. 20 (1) (2019) 251, https://doi.org/10.1186/s13059-019-1868-z.

[37] B. Kukreja, S. Jeon, W. Cao, B. Rusu, C.F. Harrison, S. Ghazisaeidi, B.T. Kalish, Spatial transcriptomics of the developing mouse brain immune landscape reveals effects of maternal immune activation and microbiome depletion, Nat. Neurosci. (2026), https://doi.org/10.1038/s41593-025-02162-3.

[38] B.Y. Ahn, R.F. Saldanha-Gama, J.J. Rahn, X. Hao, J. Zhang, N.H. Dang, D.L. Senger, Glioma invasion mediated by the p75 neurotrophin receptor (p75 (NTR)/CD271) requires regulated interaction with PDLIM1, Oncogene 35 (11) (2016) 1411–1422, https://doi.org/10.1038/onc.2015.199.

[39] J. Zhu, H. Xiao, C. Li, X. Li, J. Zheng, X. Yao, X. Zhu, PDLIM1, a novel miR-3940-5p target, regulates the malignant progression of diffuse large B-cell lymphoma, Cancer Biol. Ther. 25 (1) (2024) 2429175, https://doi.org/10.1080/15384047.2024.2429175.

[40] Y. Zhao, Y. Song, R. Zhao, M. Zhao, Q. Huang, Gene panel of persister cells as a prognostic indicator for tumor repopulation after radiation, Front. Oncol. 10 (2020) 607727, https://doi.org/10.3389/fonc.2020.607727.

[41] B. Ye, M. Yu, M. Yue, M. Yin, C. Zhang, Q. Wang, Z. Zhao, Role of PDLIM1 in hepatic stellate cell activation and liver fibrosis progression, Sci. Rep. 13 (1) (2023) 10946, https://doi.org/10.1038/s41598-023-38144-3.

[42] X. Huang, L.Z. Zhou, W.J. Feng, Y.Q. Liu, M. Chen, L.Y. Tang, P. Zhang, Circ ubiquitin-like-containing plant homeodomain and RING finger domains protein 1 increases the stability of G9a and ubiquitin-like-containing plant homeodomain and RING finger domains protein 1 messenger RNA through recruiting eukaryotic translation initiation factor 4A3, transcriptionally inhibiting PDZ and homeobox protein domain protein 1, and promotes the metastasis of hepatocellular carcinoma, J. Gastroenterol. Hepatol. 39 (3) (2024) 596–607, https://doi.org/10.1111/jgh.16408.